Nonlinear Dyn (2018) 91:591–607
https://doi.org/10.1007/s11071-017-3896-0

ORIGINAL PAPER

Optimal control of a wind turbine with digital fluid power transmission

Niels H. Pedersen · Per Johansen · Torben O. Andersen

Received: 1 September 2016 / Accepted: 21 October 2017 / Published online: 2 November 2017

Abstract Digital fluid power (DFP) technology may lead to a paradigm shift in large-scale transmission systems in, e.g., wind and wave energy. Therefore, the development of applicable control algorithms is of major importance, but is complicated by the non-smooth behavior of the DFP displacement machines. The power throughput of a full stroke operated digital displacement machine is quantized by the number of pressure chambers. The dynamics of each pressure chamber may be described by highly nonlinear continuous differential equations, whereas the input is discretely updated and binary (active or inactive). This paper contributes with a feedback control strategy for a digital displacement machine, where the binary inputs are handled by a pulse density modulator. The paper presents a linearization method of handling the many nonlinearities and thereby enabling the use of Discrete Linear Time Invariant (DLTI) control theory. The control strategy is validated for control of a digital fluid power wind turbine transmission, where both a deterministic and a stochastic optimal controllers are synthesized. The study is based on the NREL 5-MW reference wind turbine, where its model is combined with a nonlinear model of the DFP transmission and full-field flow wind profiles are used for a realistic performance evaluation scenario. By simulation, it is found that the performance of the optimal controllers using the DFP transmission is similar to that of the NREL controller using a conventional transmission.

Keywords Optimal control · Wind turbine · Digital displacement · Fluid power · Hydrostatic transmission

1 Introduction

In recent years, the development of energy efficient fluid power systems is receiving an increasing interest, both with regard to conventional cylinder drives [18,48] and power take-off systems [32–34,36,45]. In this context, digital fluid power is a promising technology, due to high efficiency and superb scalability. Digital fluid power technology is characterized by the use of electrical actuated on/off valves. In order to enable this technology further, design optimization of these on/off valves is receiving a large amount of attention [40,41,43,47,55–59]. The use of digital valves entail challenges with respect to non-smooth dynamical behavior, which increases pressure oscillations [7–9] and complicates model-based feedback control development.

A research area within digital fluid power is the digital displacement technology®, which has a large potential in wind and wave energy transmission systems, since it benefits of being continuous variable and mechanical decoupled. The technology has, however, also been applied in various other fields, e.g. vehicle drive trains, suspensions and excavators [2,10,50,53].

N. H. Pedersen (✉) · P. Johansen · T. O. Andersen
Fluid Power and Mechatronic Systems, Department of Energy Technology, Aalborg University, Aalborg, Denmark
e-mail: nhp@et.aau.dk

Digital displacement machines are characterized by having a modular construction with numerous displacement chambers controlled by electrical actuated on/off valves. A comprehensive description of the digital displacement technology and development history is documented in several publications [22,33,37].

A significant amount of research has been conducted in the field of dynamic behavior and control of electro-hydraulic servo systems [6,46,60]. However, the non-smooth behavior of the digital displacement machine complicates dynamic system analysis and control development. So far control of digital displacement machines is mostly limited to small-scale applications in an open-loop configuration and often at simplified load conditions with fixed speed operation. Ehsan et al. [22] present a full stroke pressure and flow valve timing control method, where the chamber actuation decision is based on a displacement volume estimation. A look-ahead angle accounting for the response delay is included to improve the method. Using a similar control strategy, the displacement volume estimation method has been extended to include the oil compressibility by Heikkilä and Linjama [10]. Xubin [50] presents a five-level flow control strategy including both full and partial stroke operation, where the valve activation sequence is preprogrammed based on the flow requirement. Armstrong and Yuan [1] describes a multi-level control strategy for speed control of a digital fluid power motor. The outer control level consists of a velocity PI-controller, while the inner control level identifies the optimal cylinder actuation sequence, based on an estimate of the motor torque output using all the possible combination of active/inactive chambers. Johansen et al. [13] uses a full stroke delta-sigma modulation control strategy in a closed-loop configuration. The author also presents a flow control strategy using a discrete linear time invariant model-based design approach [14]. Sniegucki et al. [49] presents a torque control strategy using full stroke. The controller synthesis features a mixed logical dynamic system representation, which is used to setup a constrained optimization problem. Despite yielding improved steady-state accuracy and reduced torque ripples compared to pulse density modulation strategies, the method only allows for offline optimization.

The literature concerning digital fluid power transmissions for wind turbines is very limited and is mostly comprised by patents from Mitsubishi Heavy Industries Ltd. [25–30]. The documented control strategies are open-loop and based on estimation techniques, from where system stability and disturbance rejection ability is unknown.

In this work, a feedback control strategy for a wind turbine with a digital fluid power transmission is presented, since the digital displacement machines have a high potential for use in large-scale transmission systems. A delta-sigma pulse density modulator is used to determine the actuation sequence of the full stroke operated pressure chambers of the digital displacement motor. The discrete operation of the digital motor complicates a dynamic analysis of the system and the use of feedback control. Additionally, highly nonlinear effects are introduced by the stochastic wind speed and turbine characteristics, as well as the digital motor and pulse density modulator. Therefore, a linear approximation of the system equations is made, allowing for use of linear optimal feedback control.

2 System description

2.1 Turbine and transmission system

The digital fluid power transmission system for the wind turbine comprises a conventional fixed displacement pump, a high- and low-pressure line and a variable digital displacement motor as illustrated in Fig. 1.

The wind turbine model has the wind speed, v, and the blade pitching angle, β, as inputs and output the aerodynamic rotor torque, τ_r, driving a fixed displacement pump. The hydraulic pump outputs a pressurized fluid flow, Q_p, and the digital motor flow intake, Q_m, is controlled by the motor displacement fraction, α_m. The high-pressure motor fluid flow is further converted into a shaft rotation of the generator.

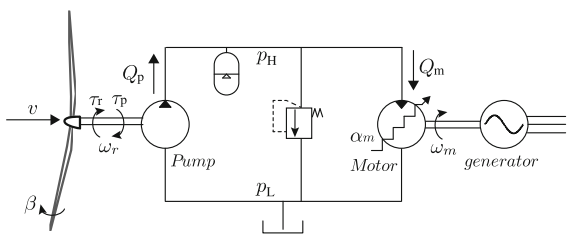

Fig. 1 Illustration of the digital fluid power transmission for a wind turbine

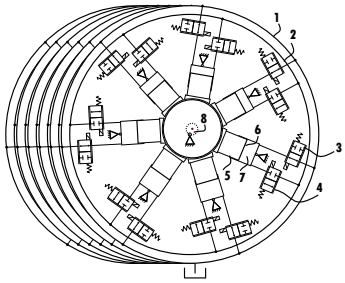

Fig. 2 Schematic of the digital displacement motor with 42 pressure chambers. The sketch is based on work by [49]

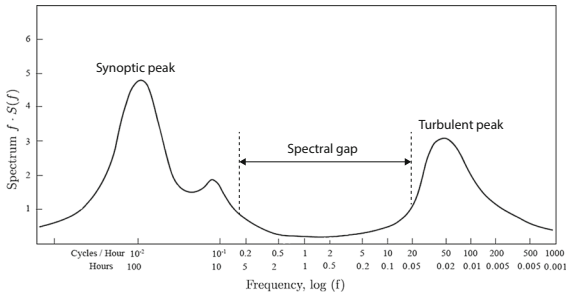

Fig. 3 Van der Hoven power spectrum of horizontal wind speeds [11]

With application control of a digital displacement unit being the main objective of this study, several simplifications to the system have been made. The hydraulic accumulator in the high-pressure line and the external boost system controlling the low pressure is omitted. Furthermore, it is assumed that the motor speed is constant since an ideal synchronous generator is considered. A digital displacement pump could be used for more advanced control strategies than the one presented, but is for simplicity not considered in this study.

2.2 Digital displacement motor

The digital displacement motor is a radial piston type, where the design under consideration consists of 6 modules with 7 cylinders in each module. An actively controlled high- and low-pressure digital valve (HPV and LPV) controls the flow throughput between the cylinder chamber and the high- and low-pressure line, respectively. A reciprocating piston motion is generated by the pressurized fluid flow and takes place since each piston is connected to a common eccentric shaft. A simplified illustration of the digital displacement motor is shown in Fig. 2.

In a full stroke operation, each displacement chamber is either using an idling (Inactive) or a motoring (Active) stroke during a shaft revolution. In an idling stroke, the HPV is kept closed and the LPV is kept open during the full revolution, resulting in a low chamber pressure and thus no work. During a motoring stroke, the low-pressure valve is closed and the high-pressure valve is opened during the intake part of the stroke, where high-pressure fluid flow enters the pressure chamber and drives the motor shaft. The displacement fraction input, α_m, is hence the fraction of activated cylinders and thus determines the amount of pressurized fluid flow used to drive the motor shaft. A pumping stroke is not considered in this work, since the motor displacement reference is positive during normal operation.

3 Mathematical modeling

The system model comprises a turbulent wind model, a simplified model of the turbine main dynamics and aerodynamic efficiency, as well as a model of the hydrostatic transmission, including the digital fluid power motor.

3.1 Turbulent wind model

Full-field flow time-series data of the wind speed are given as input to the turbine model. The data are generated by use of the open-source software TurbSim by NREL [15,16], where the IEC 61400-1 normal turbulence model and Kaimal turbulence spectrum are utilized. A low turbulence intensity of 12 % is arbitrary chosen since offshore operation at no specific site is considered.

To include the stochastic wind disturbance effect in the control design, a nonlinear model of the turbulence wind speed is presented. The wind speed may be divided into two distinct components given as

$$v(t) = \bar{v} + \Delta v(t) \tag{1}$$

where $\bar{v}$ is the slowly varying mean wind speed and $\Delta v(t)$ is the rapidly varying turbulent component being a stochastic process. These two distinct components may also be viewed on the Van der Hoven power spectrum shown in Fig. 3.

For time-series data of the wind speed of less than 10 minutes, the synoptic peak corresponding to the macro-meteorology mean wind speed may be treated as constant. The analytical Kaimal power spectrum model is used to describe the turbulent part and is given by Eq. (2). The model is provided in accordance with the IEC 61400-1 standard [3], and is a modification of the spectrum originally presented by Kaimal et al. [19].

$$\mathcal{S}(f) = \frac{4\,\sigma_{\mathrm{u}}^2\,\frac{L_{\mathrm{u}}}{\bar{v}}}{\left(1+6\,\frac{L_{\mathrm{u}}}{\bar{v}}\,f\right)^{5/3}} \tag{2}$$

where σ_{u} and L_{u} are the standard deviation and scale parameter, respectively, and are specified in IEC 61400-1 [3] as functions of the turbulence intensity. For a 12 % turbulence intensity $\sigma_{\mathrm{u}} = 1.94$ and $L_{\mathrm{u}} = 340.2$. In this study, a mean wind speed of $\bar{v} = 8$ m/s has been chosen since it corresponds to approximately the midpoint of operation region II, where the transmission is used to control the extracted wind energy (An elaboration of this is documented in Sect. 4).

3.2 Wind turbine model

The wind turbine considered in this study is the National Renewable Energy Laboratory (NREL) 5-MW reference turbine. Its model is combined with the dynamical model of the digital fluid power transmission through the use of a MATLAB/Simulink interface. The dynamics and aero-elastic effects of the wind turbine are simulated by use of the open-source program FAST (Fatigue, Aerodynamics, Structures and Turbulence program) [17], which model is based on the blade element momentum theory. For control purpose, a simplified nonlinear model is derived for the main turbine dynamics. Additionally, a static description of the aerodynamic power P_{r} and torque τ_{r} is used and is given by Eqs. (3) and (4), respectively.

$$P_{\mathrm{r}} = \frac{1}{2}\,A_{\mathrm{r}}\,\rho_{\mathrm{air}}\,C_{\mathrm{p}}\,(\lambda,\beta)\;v^3 \tag{3}$$

$$\tau_{\mathrm{r}} = \frac{1}{2}\,A_{\mathrm{r}}\,R_{\mathrm{r}}\,\rho_{\mathrm{air}}\,C_{\mathrm{q}}\,(\lambda,\beta)\;v^2 \tag{4}$$

where A_{r} and R_{r} describe the rotor swept area and radius, respectively, and ρ_{air} is the air density. $C_{\mathrm{p}}\,(\lambda,\beta)$ and $C_{\mathrm{q}}\,(\lambda,\beta)$ are the turbine specific power and torque coefficient, which are nonlinear functions with respect to the tip-speed ratio, λ, and blade pitch angle, β. The tip-speed ratio is defined in Eq. (5) and describes the ratio between the tip-speed of the blades and the wind speed.

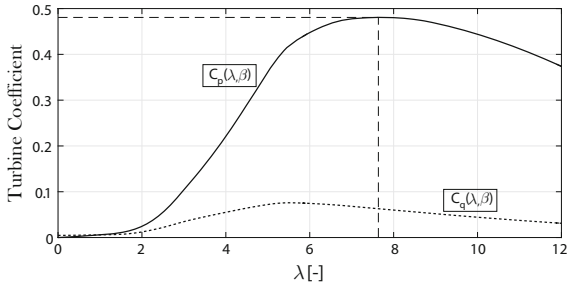

Fig. 4 Power and torque coefficient as a function of tip-speed ratio at the maximum power pitching angle for the NREL 5 MW turbine

$$\lambda = \frac{\omega_r\,R_r}{v} \tag{5}$$

The nonlinear turbine coefficients C_{p} and C_{q} are used actively for optimal power control of the turbine. A plot of the turbine coefficients as a function of the tip-speed ratio at the maximum power pitch angle is shown in Fig. 4.

The maximum power coefficient is identified to be $C_{\mathrm{p}}^* = 0.485$ and occurs at a tip-speed ratio of $\lambda^* = 7.55$. This information is used in the control structure described later in Sect. 4 to maximize the power capture below rated wind speed.

A simplified model of the turbine dynamics is derived to be that given by

$$\dot{\omega}_{\mathrm{r}} = \frac{1}{J_{\mathrm{r}}}\left(\tau_{\mathrm{r}} - d_{\mathrm{r}}\,\omega_{\mathrm{r}} - \underbrace{\frac{\bar{V}_{\mathrm{p}}\,\Delta p}{\eta_{\mathrm{p}}}}_{\tau_{\mathrm{p}}}\right) \tag{6}$$

where J_{r} describes the combined mass moment of inertia of the turbine rotor consisting of the blades, shaft and hub. d_{r} is the viscous friction coefficient of the rotor shaft, $\bar{V}_{\mathrm{p}}$ is the pump displacement volume per radians and η_{p} is the mechanical efficiency coefficient, which includes the static friction of the shaft.

Table 1 Parameters of the NREL 5 MW

Parameter	Symbol	Value	Unit
Cut-in wind speed	v_{in}	4	m/s
Rated wind speed	v_{r}	11.4	m/s
Cut-out wind speed	v_{out}	25	m/s
Air density	ρ_{air}	1.225	kg/m^3
Blade radius	R_{r}	63	m
Rotor swept area	A_{r}	12469	m^2
Tower height	h_{t}	90	m
Rated rotor speed	$\omega_{\text{r-nom}}$	12.13	rpm
Rotor and shaft inertia	J_{r}	3.87e7	kg m^2
Viscous friction	d_{r}	50e3	N m s $/rad$
Optimal tip-speed ratio	λ^*	7.55	–
Maximum power coefficient	C_{p}^*	0.485	–

The main parameters of the NREL 5-MW wind turbine are provided in Table 1.

3.3 Hydrostatic transmission model

The low-pressure line is simplified to be constant, since it may be externally controlled by a boost pump circuit. Defining the pressure difference as $\Delta p = p_{\text{H}} - p_{\text{L}}$, its dynamics is described by

$$\dot{\Delta}_{\text{p}} = \frac{\beta_{\text{e}}}{V_{\text{H}}} \left(\underbrace{\bar{V}_{\text{p}}\, \omega_{\text{r}}}_{Q_{\text{p}}} - Q_{\text{m}} - k_{\text{l}}\, \Delta_{\text{p}} \right) \tag{7}$$

where β_{e} is the effective oil bulk modulus, V_{H} is the volume of the high-pressure line and k_{l} is the leakage coefficient between the high- and low-pressure lines.

3.4 Digital displacement motor

The utilized mathematical model of the digital machine is inspired by Roemer [39] and is based on the schematic of a single cylinder chamber shown in Fig. 5.

V_c is the chamber volume and A_{p} is the piston area. The piston displacement x_{p} as a function of the shaft rotation angle θ is described by Eq. (8), where r_{e} is the eccentric radius.

$$x_{\text{p}}(\theta) = r_{\text{e}}\ (1 - \cos\theta) \tag{8}$$

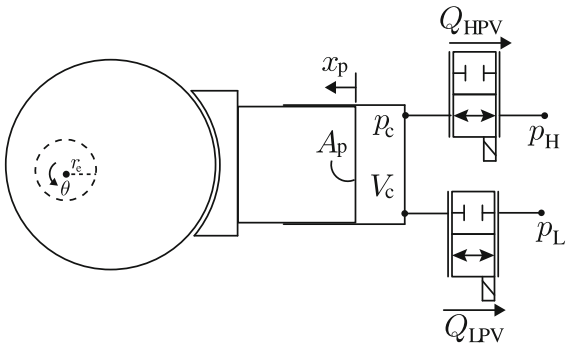

Fig. 5 Schematic of a single pressure chamber with definition of model variables

With the piston displacement volume described by $V_{\text{d}} = 2\, r_{\text{e}}\, A_{\text{p}}$, the chamber volume and its time derivative is given as

$$V_{\text{c}}(\theta) = \frac{V_{\text{d}}}{2}\ (1 - \cos\theta) + V_0 \quad \dot{V}_{\text{c}}(\theta) = \frac{V_{\text{d}}}{2}\ \dot{\theta}\ \sin\theta \tag{9}$$

where V_0 is the minimum chamber volume. Applying the continuity equation to the pressure chamber, its pressure p_{c} is described by

$$\dot{p}_{\text{c}} = \frac{\beta_{\text{e}}}{V_{\text{c}}} \left(Q_{\text{HPV}} - Q_{\text{LPV}} - \dot{V}_{\text{c}} \right) \tag{10}$$

By use of the orifice equation, the flow through the high- and low-pressure valves (Q_{HPV} and Q_{LPV}) are expressed as

Table 2 Parameters of the hydrostatic transmission

Parameter	Symbol	Value	Unit
Pump mechanical efficiency	η_p	0.95	–
Fixed pump displacement	$\bar{V}_p$	121.88	L/rad
Pipeline length	l_p	10	m
Pipeline internal diameter	d_p	100	mm
Transmission line volume	V_H	78.54	L
Effective bulk modulus	β_e	16000	bar
Transmission leakage coefficient	k_l	0.1	L/bar
Low pressure	p_L	5	bar
Synchronous motor speed	ω_m	1500	rpm
Motor piston area	A_p	79	cm^2
Motor eccentric radius	r_e	37.5	mm
Motor displacement volume	V_d	498.57	cm^3
Chamber flow coefficient	k_f	$0.5 \cdot 10^5$	$\sqrt{pa}\ s/m^3$
Valve actuation time	t_s	1	ms
HPV closing angle	$\theta_{H\text{-}cl}$	148.2	deg
LPV closing angle	$\theta_{L\text{-}cl}$	334.7	deg
Nominal pressure	Δp_{nom}	350	bar
Nominal rotor torque	$\tau_{r\text{-}nom}$	4.25	MN m

$$\begin{aligned} Q_{HPV} &= \frac{\bar{x}_H}{k_f}\sqrt{|p_H - p_c|}\,\mathrm{sign}\,(p_H - p_c) \\ Q_{LPV} &= \frac{\bar{x}_L}{k_f}\sqrt{|p_c - p_L|}\,\mathrm{sign}\,(p_c - p_L) \end{aligned} \tag{11}$$

where $\bar{x}_H$ and $\bar{x}_L$ are normalized valve plunger positions of the high- and low-pressure valve, respectively, and k_f is the valve flow coefficient. The valve dynamics is simplified to be described as a constant plunger acceleration given in Eq. (12) for valve opening. The constant acceleration approximation omits the dynamic description of the actuation and fluid forces, as well as the stiction effects [31,42,44], which entail impractical and long simulation durations.

$$a_{v+} = \begin{cases} 4/t_s^2 & for \quad 0 \le t \le t_s/2 \\ -4/t_s^2 & for \quad t_s/2 \le t \le t_s \end{cases} \tag{12}$$

where t_s is the valve opening/closing time. The constant acceleration results in a smooth plunger position with a maximum velocity at the midpoint between fully closed and open. The valve closing is similar described as $a_{v-} = -a_{v+}$.

The motor flow intake Q_m is the sum of flows through each individual high-pressure valve given by

$$Q_m = \sum_{i=1}^{N} Q_{HPV}(i) \tag{13}$$

where $N = 42$ is the number of pressure chambers. The parameter values used in the mathematical model of the hydrostatic transmission are provided in Table 2.

3.5 DDM operation strategy and simulation results

The digital valves are controlled by actively closing them at an angle of $\theta_{H\text{-}cl}$ and $\theta_{L\text{-}cl}$ for the high- and low-pressure valve, respectively. Passive valve opening is utilized where the high-pressure valve is opened due to pressure force when $p_c > p_H$ and the low-pressure valve is opened due to suction when $p_c < p_L$. Simulation results of a pressure chamber for a motoring and an idling stroke are shown in Fig. 6 For the idling stroke, the high-pressure valve is kept closed and the low pressure valve is kept open during a full revolution, resulting in no chamber pressurization. For the

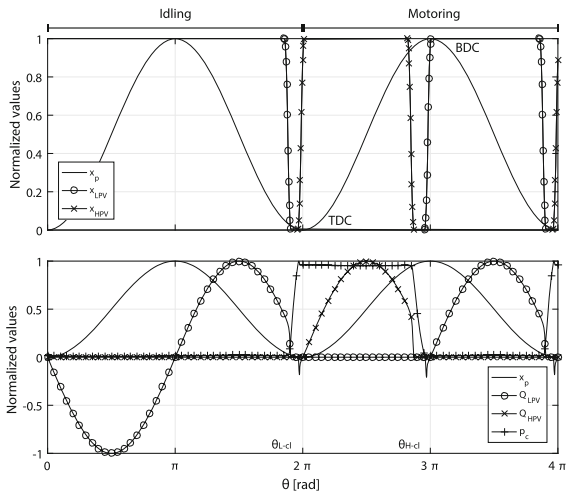

Fig. 6 Simulation results for a single pressure chamber

motoring stroke, the low-pressure valve is closed at $\theta_{\text{L-cl}}$ near top dead center (TDC), resulting in a pressure build up, followed by a passive opening of the high-pressure valve. A backflow into the high-pressure line is created momentarily due to the chamber pressure exceeding the high pressure. During the intake stroke part, high-pressure oil is entering the pressure chamber and thereby driving the piston and eccentric. Near bottom dead center (BDC) at $\theta_{\text{H-cl}}$, the high-pressure valve is actively closed causing a de-pressurization due to piston extension. This further results in a passive opening of the low-pressure valve due to suction.

Since the pressure chamber dynamics is very fast compared to that of the wind turbine, the pressure chamber model has been solved for various high pressures and the results has been implemented in a look-up table for a significantly reduction is simulation time.

4 Wind turbine operation and control objectives

The conventional operation strategy for a variable-speed variable-pitch wind turbine is divided into four regions dependent on the wind speed. In this paper, the turbine control has been limited to region II between cut-in wind speed, v_{in}, and rated wind speed, v_{r}, since the turbine is solely controlled by the transmission system in this region. Therefore, the pitching system and control of it is not investigated in the presented work.

4.1 Region II control

In the outer turbine control level, the popular $k\,\omega^2$ control law is used, which yield a good compromise between maximum power capture and rotor torque fluctuations. It is found in Fig. 4 that the maximum power capture is obtained by maintaining the optimal tip-speed ratio, λ^*, yielding the maximum power coefficient C_{p}^*. Combining this information with the static rotor torque equation in Eq. (4) and the fact that $C_{\text{p}}(\lambda,\beta) = \lambda\, C_{\text{q}}(\lambda,\beta)$, the $k\,\omega^2$ control law is derived to be that given by

$$\begin{aligned} \tau_{\text{r}} &= \frac{1}{2}\, A_{\text{r}}\, R_{\text{r}}\, \rho_{\text{air}}\, \frac{C_{\text{p}}(\lambda,\beta)}{\lambda} \left(\frac{R_{\text{r}}\,\omega_{\text{r}}}{\lambda}\right)^2 \\ \tau_{\text{r}}^* &= \underbrace{\frac{1}{2}\, A_{\text{r}}\, R_{\text{r}}^3\, \rho_{\text{air}}\, \frac{C_{\text{p}}^*}{\lambda^{*3}}}_{K_2}\, \omega_{\text{r}}^2 \end{aligned} \tag{14}$$

The rotor torque reference τ_{r}^* is thus only a function of the rotor speed ω_{r}, why the high-frequency wind speed fluctuations are filtered away in the control law, at the cost of a minor reduction in optimal tip-speed ratio tracking. Since the rotor torque in this study is controlled by the DFP transmission, the rotor torque reference is converted into a difference pressure reference by static use of Eq. (6) resulting in

$$\Delta_{\text{p}}^* = \left(\tau_{\text{r}}^* - d_{\text{r}}\,\omega_{\text{r}}\right) \frac{\eta_{\text{p}}}{\bar{V}_{\text{p}}} \tag{15}$$

4.2 Wind turbine control structure

The proposed control structure takes basis in the objective of accurately controlling the difference pressure, Δ_{p}, by the motor displacement fraction, α_{m}, using a full stroke operation strategy and state feedback. The proposed feedback control strategy is shown in Fig. 7 and is similar to that applied for a conventional fluid power wind turbine transmission by various authors [5,21,54].

A pressure controller is seen to act on the pressure reference, Δ_{p}^*, based on the measured states, Δ_{p} and ω_{r} and output a motor displacement fraction reference α_{m}^* being between 0 and 1. The displacement reference is converted into a pressure chamber activation sequence by a delta-sigma pulse density modulator, determine whether the current cylinder chamber should use a

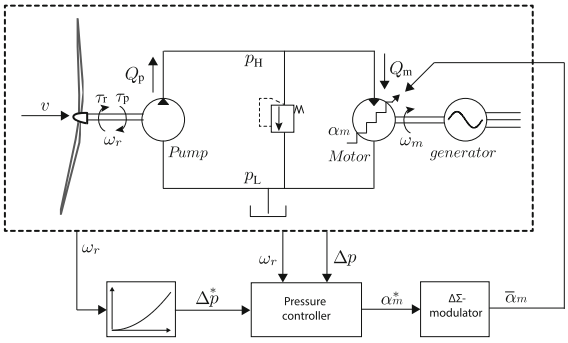

Fig. 7 Control structure for hydrostatic wind turbine transmission

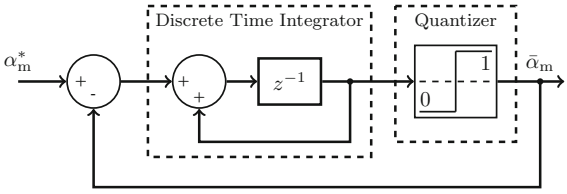

Fig. 8 First-order delta sigma Modulation block diagram

motoring or an idling stroke as proposed by Johansen et al. [13]. The chamber activation sequence $\bar{\alpha}_m$ is thus a binary signal, which time average output is equal to the displacement fraction reference.

The decision to either use a motoring (Active) or an idling (Inactive) stroke is performed once every revolution for each cylinder. As a consequence, the system nature implies use of discrete control. The discrete sampling time, T_s, is therefore dependent on the motor rotation speed and the number of cylinders given as

$$T_s = \frac{2\,\pi}{\omega_m\, N} \tag{16}$$

where $\omega_m = \dot{\theta}$ is the motor rotational speed, such that $T_s = 0.952\,\text{ms}$ for $\omega_r = 1500\,\text{rpm}$. This corresponds to a decision for every $\theta_s = 2\,\pi/N = 8.6°$ of shaft angle rotation.

4.3 Delta-sigma modulator

A discrete first-order DSM is utilized in this study, but theoretically any 1 bit analog-to-digital converter may be used. A block diagram representation of the discrete first-order DSM is shown in Fig. 8.

The modulator consists of a discrete time integrator and a quantizer in a feedback structure. The integrator is hence acting on the displacement fraction error and thereby yielding a time average approximation of the input. As a result, the quantizer of the modulator introduces an additional high nonlinearity to the control system.

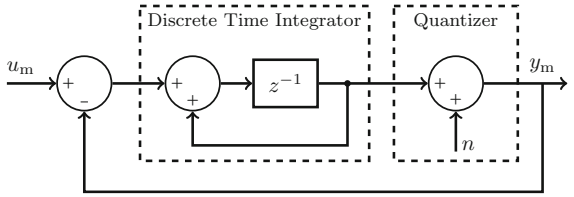

Fig. 9 Linear representation of delta sigma Modulator

5 Linear model approximation

It is evident that the system comprises a number of severe nonlinearities and stochastic disturbance effects. Stochastic optimal control of nonlinear systems is a mature field with numerous applications [12,24,51]. Both continuous and discrete stochastic linear optimal control has been successfully applied for control of variable-speed wind turbines [20,23,35]. On this basis, linear optimal control is the strategy of choice in present study. However, the use of optimal linear control of digital displacement machines is a new field and is unconventional since most of the states are binary, which becomes evident in the following section. In consequence, a linear approximation of the system nonlinearities is derived and used to set up a state model describing the system dynamics.

5.1 Delta-sigma modulator

The modulator may be considered linearly by assuming the quantizer as an additive noise input n as illustrated in Fig. 9.

The noise input is hence a time varying value between $\pm$ 0.5 describing the discretization error. A linear transfer function representation of the modulator is derived to be that given as

$$\begin{aligned} Y_m(z) &= \frac{1}{z}\,U_m(z) + \frac{z-1}{z}\,N(z) \\ y_m(k) &= u_m(k-1) + n(k) - n(k-1) \end{aligned} \tag{17}$$

The output of the linear representation of the first-order DSM is hence a single sampled delayed input together with the noise input discrete differentiated.

The quantization error noise $n(k)$ may be described as a white noise source with intensity Q_m in accordance with Reiss et al. [38]. For a one bit quantizer, the discretization step size is $q = 1$, resulting in the quantization error span $-\frac{q}{2} \leq e_\mathrm{q} \leq -\frac{q}{2}$. The noise error may be assumed to be statistically described by a uniform distribution function with mean error $\bar{e}_\mathrm{q} = 0$. The noise power is then identified by investigating the quantizer error variance determined by

$$\sigma_\mathrm{e}^2 = E\{(e_\mathrm{q} - \bar{e}_\mathrm{q})^2\} = \frac{1}{q}\int_{-q/2}^{q/2} e_\mathrm{q}^2 de_\mathrm{q} = \frac{q^2}{12} \tag{18}$$

Since the quantizer disturbance is to be described with a white noise input, the power spectral density of it is also uniformly distributed across the frequency range of the Nyquist band. The power spectral density function of the quantization noise then becomes

$$\Phi_\mathrm{e}(f) = \frac{\sigma_\mathrm{e}^2}{f_\mathrm{s}} = Q_\mathrm{d} \tag{19}$$

where $f_\mathrm{s} = 1050\,\mathrm{Hz}$ is the sampling frequency. The error noise filter is therefore given by $n(k) = \sqrt{Q_\mathrm{d}}\, w_2(k)$, where $w_2(k)$ is a white noise input having unity intensity. Inserting this expression into the linear discrete modulator model given in Eq. (17) yields

$$y_\mathrm{m}(k) = u_\mathrm{m}(k-1) + \sqrt{Q_\mathrm{d}}\, w_2(k) - \sqrt{Q_\mathrm{d}}\, w_2(k-1) \tag{20}$$

In conventional stochastic optimal control, it is assumed that the disturbance is Gaussian white noise having a normal distribution. Despite the modulator noise having a uniform distribution function, the estimator to be designed is still the optimal linear one [4].

5.2 Digital fluid power motor

The non-smooth behavior of the digital fluid power flow dynamics complicates the construction of a linear approximation by the conventional first-order Taylor series expansion method. Alternatively, in this study an approach based on a direct discrete linear approximation of the continuous non-smooth motor dynamics is used to overcome this difficulty. The model is derived by approximating each motor flow between samples by

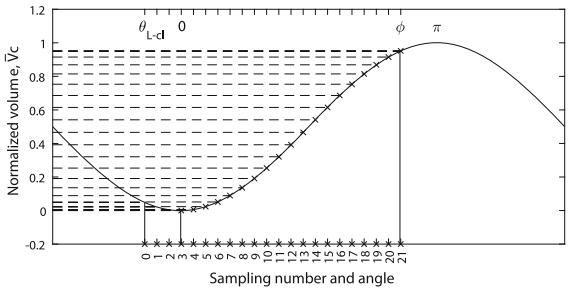

Fig. 10 Illustration of motor displacement fraction output as a function of sampling number

Eq. (21) and thereby neglecting the transient pressure dependency.

$$Q_\mathrm{HPV} \approx \frac{dV_\mathrm{c}(\theta(t))}{dt}$$
$$Q_\mathrm{HPV}[k] \approx \frac{V_\mathrm{d}}{T_\mathrm{s}}\left(\bar{V}_\mathrm{c}(\theta[k+1]) - \bar{V}_\mathrm{c}(\theta[k])\right) = \frac{V_\mathrm{d}}{T_\mathrm{s}}\,\Delta\bar{V}_\mathrm{c}[k] \tag{21}$$

where $\bar{V}_\mathrm{c}$ is the normalized displacement volume. The discrete motor model is derived based on Fig. 10, showing the normalized displacement volume as a function of sampling number and shaft angle.

With 42 pressure chambers, a full motoring stroke ideally last for 21 samples between $0 \leq \theta \leq \pi$. Due to valve actuation dynamics, $\theta_\mathrm{L\text{-}CL}$ is located ahead of this and two delay samples are introduced such that motoring starts just before sample $k = 3$. Sample $k = 0$ is the chamber activation decision sample and thus lies at $\theta_\mathrm{L\text{-}CL}$.

Since the HPV must be closed in time for the LPV to be fully open at $\theta = \pi$, it is not possible to utilize a full motoring stroke. ϕ indicates the angle where the high-pressure valve is half way closed, which is the midpoint angle between $\theta_\mathrm{H\text{-}CL}$ and the angle where the valve becomes fully closed. ϕ should hence correspond to the best discrete estimate of when motoring stops.

The motor displacement fraction, α_m, is described by a sum of displacement fractions between samples during motoring based on the convolution sum method presented by Johansen et al. [14] and is given in Eq. (22). Also, an expression for the approximated motor flow is provided.

$$\alpha_\mathrm{m}[k] = \sum_{m=0}^{k} \Delta\bar{V}_\mathrm{c}[k-m]\,\bar{\alpha}_\mathrm{m}[m]$$

$$Q_{\mathrm{m}}[k] = \underbrace{\frac{V_{\mathrm{d}}}{T_{\mathrm{s}}}}_{k_{\mathrm{q}}} \alpha_{\mathrm{m}}[k] \tag{22}$$

where the displacement fractions are calculated by Eq. (23), which may be validated from Fig. 10.

$$\Delta \bar{V}_{\mathrm{c}}[k] = \begin{cases} 0 & \theta[k], \theta[k+1] \notin [0\,;\phi] \\ \bar{V}_{\mathrm{c}}(\theta[k+1]) - \bar{V}_{\mathrm{c}}(\theta[k]) & \theta[k], \theta[k+1] \in [0\,;\phi] \\ \bar{V}_{\mathrm{c}}(\theta[k+1]) - \bar{V}_{\mathrm{c}}(0) & \theta[k] < 0 < \theta[k+1] \\ \bar{V}_{\mathrm{c}}(\phi) - \bar{V}_{\mathrm{c}}(\theta[k]) & \theta[k] < \phi < \theta[k+1] \end{cases} \tag{23}$$

It is seen that the displacement fraction is 0 outside the interval $\theta = [0\,;\phi]$, resulting in it being 0 outside the sampling interval $k = [2\,;20]$.

A comparison of the digital motor flow described by the discrete linear approximation model and the non-linear dynamic model is shown in Fig. 11.

The discrete linear model approximation is seen to have a great accuracy, with the exception that it does not include valve and pressure dynamics, why the back-flow is not seen. Due to the fairly high accuracy in the majority of the motor stroke, the linear approximation is considered validated and used to describe the digital motor flow when designing controllers.

5.3 Turbulent wind model

The turbulence wind speed is modeled as a linear filter with white noise input given by $v(t) = H_{\mathrm{v}}(t)\, w_1(t)$, where the white noise has intensity Π_{v}. The power spectrum of the output $v(t)$ of the linear model is given by Eq. (24).

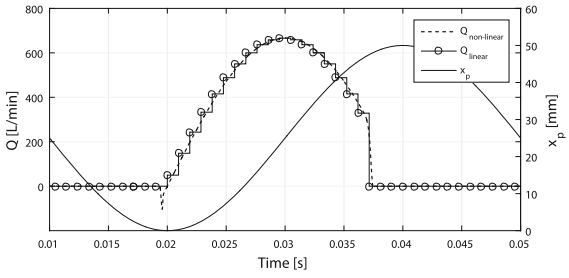

Fig. 11 Comparison of the linear and nonlinear model of the digital motor flow

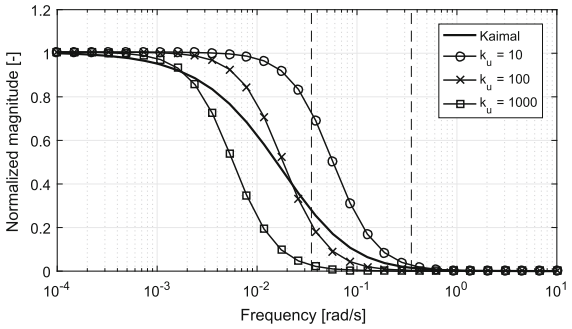

Fig. 12 Normalized magnitude of the Kaimal spectrum and approximations. (Dashed lines indicates desired frequency band)

$$\Phi_{\mathrm{v}}(\omega) = H_{\mathrm{v}}(j\,\omega)\, \Pi_{\mathrm{v}}\, H_{\mathrm{v}}(-j\,\omega) \tag{24}$$

A linear approximation of the power spectrum is thus necessary and is derived to be that in Eq. (25), based on the approach described by Vepa [52].

$$\Phi_{\mathrm{v}}(\omega) = \frac{4\,\sigma_{\mathrm{u}}^2\,\frac{L_{\mathrm{u}}}{\bar{v}}}{\left(1 + 6\,\frac{L_{\mathrm{u}}}{2\,\pi\,\bar{v}}\,\omega\right)^{5/3}} \approx \frac{4\,\sigma_{\mathrm{u}}^2\,\frac{L_{\mathrm{u}}}{\bar{v}}}{\left(1 + k_{\mathrm{u}}\left(\frac{\omega}{\omega_{\mathrm{c}}}\right)^2\right)} \tag{25}$$

where $\omega_{\mathrm{c}} = 2\pi\,\bar{v}/L_{\mathrm{u}}$ and k_{u} is a frequency factor specifying at which frequency the approximation is most accurate. From the Van der Hoven frequency spectrum of the wind shown in Fig. 3, it is identified that the turbulent peak has a frequency band between 20 and 200 cycles/hour, corresponding to $0.035 \leq \omega \leq 0.35$ rad/s. The optimal frequency factor is determined from the semi-logarithmic plot of the normalized power spectrum function shown in Fig. 12.

A reasonable approximation for the desired frequency band is found for $k_{\mathrm{u}} = 100$. By using Eq. (24) and Eq. (25), it is derived that the state representation of the linear filter is given by Eq. (26) when the white noise input has unity intensity.

$$\dot{v} = \underbrace{-\frac{\omega_{\mathrm{c}}}{\sqrt{k_{\mathrm{u}}}}}_{a_v}\, v + \underbrace{2\,\omega_{\mathrm{c}}\,\sigma_{\mathrm{u}}\sqrt{\frac{L_{\mathrm{u}}}{k_{\mathrm{u}}\,\bar{v}}}}_{b_v}\, w_1 \tag{26}$$

5.4 Aerodynamic rotor torque

A linear approximation by first-order Taylor expansion of the aerodynamic rotor torque is derived to be that given as

$$\begin{aligned}\delta\tau_\mathrm{r} &= \underbrace{\left(\frac{d\tau_\mathrm{r}}{dv}\left(\frac{1}{2}\,A_\mathrm{r}\,R_\mathrm{r}\,\rho_\mathrm{air}\,C_\mathrm{q}\,(\lambda,\beta)\;v^2\right)|_{v=\bar{v},\lambda=\lambda^*,\beta=0}\right)}_{k_{\tau v}}\,\delta v\\ k_{\tau v} &= A_\mathrm{r}\,R_\mathrm{r}\,\rho_\mathrm{air}\,C_\mathrm{q}(\lambda^*,0)\,\bar{v}\\ \delta\tau_\mathrm{r} &= k_{\tau v}\,\delta v \longrightarrow \delta v = k_{\tau v}^{-1}\,\delta\tau_\mathrm{r}\end{aligned} \tag{27}$$

By combining Eqs. (26) and (27), the linear model of the rotor torque described as filtered white noise is given as

$$\dot{\tau}_\mathrm{r} = -a_v\,\tau_\mathrm{r} + k_{\tau v}\,b_v\,w_1 \tag{28}$$

6 State model representation

To allow for discrete optimal control, a discrete state representation of the system dynamical equations is required. Therefore, the continuous transmission and turbine model is initially discretized and afterward combined with the discrete motor and modulator models.

6.1 State-space representation

The linear continuous state-space representation of the turbine and transmission dynamics is given in Eq. (29) and is obtained by combining Eqs. (6), (7) and (28).

$$\begin{aligned}\underbrace{\begin{bmatrix}\dot{\omega}_\mathrm{r}\\ \dot{\Delta}_\mathrm{p}\\ \dot{\tau}_\mathrm{r}\end{bmatrix}}_{\dot{\mathbf{x}}(t)} &= \underbrace{\begin{bmatrix}-\frac{d_\mathrm{r}}{J_\mathrm{r}} & -\frac{\bar{V}_\mathrm{p}}{J_\mathrm{r}\eta_\mathrm{p}} & \frac{1}{J_\mathrm{r}}\\ \frac{\beta_\mathrm{e}}{V_\mathrm{H}}\bar{V}_\mathrm{p} & -\frac{\beta_\mathrm{e}}{V_\mathrm{H}}k_\mathrm{l} & 0\\ 0 & 0 & -a_v\end{bmatrix}}_{\mathbf{A}}\underbrace{\begin{bmatrix}\omega_\mathrm{r}\\ \Delta_\mathrm{p}\\ \tau_\mathrm{r}\end{bmatrix}}_{\mathbf{x}(t)} + \underbrace{\begin{bmatrix}0\\ -\frac{\beta_\mathrm{e}}{V_\mathrm{H}}\\ 0\end{bmatrix}}_{\mathbf{B}}\underbrace{Q_\mathrm{m}}_{u(t)} + \underbrace{\begin{bmatrix}0\\ 0\\ k_{\tau v}\,b_v\end{bmatrix}}_{\mathbf{G}}w_1(t)\\ \mathbf{y}(t) &= \underbrace{\begin{bmatrix}1&0&0\\ 0&1&0\end{bmatrix}}_{\mathbf{C}}\mathbf{x}(t)\end{aligned} \tag{29}$$

To ease the controller design in the following section, the plant has been normalized by the diagonal matrix $\mathbf{H} = \mathrm{diag}\left\{\left[\omega_\text{r-nom}\;\Delta p_\text{nom}\;\tau_\text{r-nom}\right]\right\}$ containing the nominal/rated state values.

A discretization of the continuous model is performed to allow for discrete control. In the discretization approach, a zero-order hold input to the continuous plant is assumed, although the motor flow truly is time varying between samples. This approximation is, however, justified by the relative high number of cylinders. The discrete state-space representation of the transmission and turbine model is given by

$$\begin{aligned}\mathbf{x}(k+1) &= \mathbf{A}_\mathrm{p}\,\mathbf{x}(k) + \mathbf{B}_\mathrm{p}\,u(k) + \mathbf{G}_\mathrm{p}\,w_1(k)\\ \mathbf{y}(k) &= \mathbf{C}_\mathrm{p}\,\mathbf{x}(k)\\ \mathbf{A}_\mathrm{p} &= e^{\mathbf{A}\,T}\quad \mathbf{B}_\mathrm{p} = \mathbf{A}^{-1}\left(e^{\mathbf{A}\,T} - \mathbf{I}\right)\mathbf{B}\\ \mathbf{C}_\mathrm{p} &= \mathbf{C}\quad \mathbf{G}_\mathrm{p} = \mathbf{A}^{-1}\left(\mathbf{A}_\mathrm{p} - \mathbf{I}\right)\mathbf{G}\end{aligned} \tag{30}$$

The discrete convolution sum model of the digital motor derived in Eq. (22) is rewritten into state space form resulting in

$$\begin{aligned}\underbrace{\begin{bmatrix}u_\mathrm{d}(k)\\ u_\mathrm{d}(k-1)\\ u_\mathrm{d}(k-2)\\ \vdots\\ u_\mathrm{d}(k-p+1)\end{bmatrix}}_{\mathbf{x}_\mathrm{d}(k+1)} &= \underbrace{\begin{bmatrix}0&0&\cdots&0&0\\ 1&0&\cdots&0&0\\ 0&1&\cdots&0&0\\ \vdots&\vdots&\ddots&\vdots&\vdots\\ 0&0&\cdots&1&0\end{bmatrix}}_{\mathbf{A}_\mathrm{d}}\underbrace{\begin{bmatrix}u_\mathrm{d}(k-1)\\ u_\mathrm{d}(k-2)\\ u_\mathrm{d}(k-3)\\ \vdots\\ u_\mathrm{d}(k-p)\end{bmatrix}}_{\mathbf{x}_\mathrm{d}(k)} + \underbrace{\begin{bmatrix}1\\0\\0\\ \vdots\\ 0\end{bmatrix}}_{\mathbf{B}_\mathrm{d}}u_\mathrm{d}(k)\\ y_\mathrm{d}(k) &= \underbrace{k_\mathrm{q}\left[\Delta\bar{V}_\mathrm{c}[1]\;\Delta\bar{V}_\mathrm{c}[2]\;\Delta\bar{V}_\mathrm{c}[3]\;\cdots\;\Delta\bar{V}_\mathrm{c}[p]\right]}_{\mathbf{C}_\mathrm{d}}\mathbf{x}_\mathrm{d}(k)\\ &+ \underbrace{k_\mathrm{q}\left[\Delta\bar{V}_\mathrm{c}[0]\right]}_{\mathbf{D}_\mathrm{m}}u_\mathrm{d}(k)\end{aligned} \tag{31}$$

$p = 20$ indicates the last sampling instance with a displacement fraction $\Delta\bar{V}_\mathrm{c} \neq 0$. Also it should be noticed that $\Delta\bar{V}_\mathrm{c}[0] = \mathbf{D}_\mathrm{m} = 0$, why no direct input/output coupling is present.

By use of the discrete modulator representation in Eq. (20), the discrete modulator state model becomes

$$\begin{aligned}x_\mathrm{m}(k+1) &= \underbrace{[0]}_{A_\mathrm{m}}x_\mathrm{m}(k) + \underbrace{[1]}_{B_\mathrm{m}}u_\mathrm{m}(k) - \underbrace{\left[\sqrt{Q_\mathrm{d}}\right]}_{G_\mathrm{m}}w_2(k)\\ y_\mathrm{m}(k) &= \underbrace{[1]}_{C_\mathrm{m}}x_\mathrm{m}(k) + \underbrace{\left[\sqrt{Q_\mathrm{d}}\right]}_{V_\mathrm{m}}w_2(k)\end{aligned} \tag{32}$$

Combining the above discrete state-space representations of the various sub-systems given in Eqs. (30), (31) and (32) results in the complete discrete linear state model given by

$$\underbrace{\begin{bmatrix}\mathbf{x}(k+1)\\ \mathbf{x}_\mathrm{d}(k+1)\\ x_\mathrm{m}(k+1)\end{bmatrix}}_{\mathbf{x}_\mathrm{t}(k+1)} = \underbrace{\begin{bmatrix}\mathbf{A}_\mathrm{p} & \mathbf{B}_\mathrm{p}\,\mathbf{C}_\mathrm{d} & \mathbf{0}\\ \mathbf{0} & \mathbf{A}_\mathrm{d} & \mathbf{B}_\mathrm{d}\,\mathbf{C}_\mathrm{m}\\ \mathbf{0} & \mathbf{0} & A_\mathrm{m}\end{bmatrix}}_{\mathbf{A}_\mathrm{t}} \times \underbrace{\begin{bmatrix}\mathbf{x}(k)\\ \mathbf{x}_\mathrm{d}(k)\\ x_\mathrm{m}(k)\end{bmatrix}}_{\mathbf{x}_\mathrm{t}(k)} + \underbrace{\begin{bmatrix}\mathbf{0}\\ \mathbf{0}\\ B_\mathrm{m}\end{bmatrix}}_{\mathbf{B}_\mathrm{t}} u_\mathrm{m}(k) + \underbrace{\begin{bmatrix}\mathbf{G}_\mathrm{p} & \mathbf{0}\\ \mathbf{0} & \mathbf{B}_\mathrm{d}\,V_\mathrm{m}\\ \mathbf{0} & -G_\mathrm{m}\end{bmatrix}}_{\mathbf{G}_\mathrm{t}} \underbrace{\begin{bmatrix}w_1(k)\\ w_2(k)\end{bmatrix}}_{\mathbf{w}(k)} \quad \mathbf{y}_\mathrm{t}(k) = \underbrace{\begin{bmatrix}\mathbf{C}_\mathrm{p} & \mathbf{0} & \mathbf{0}\\ \mathbf{0} & \mathbf{I} & \mathbf{0}\end{bmatrix}}_{C_\mathrm{t}} \mathbf{x}_\mathrm{t}(k) \tag{33}$$

A full-state observer is to be designed for the stochastic controller, why as much information as possible is provided to the observer. Therefore, all the states except the two states driven by white noise are chosen as outputs.

6.2 Control feedback and integral state

Since linear control theory is to be used, a linearization of the $K\,\omega^2$ law given in Eq. (14) is necessary. A linear expression of the pressure reference given in Eq. (15) is derived to be that in Eq. (34).

$$\begin{aligned}\Delta_\mathrm{p}^* &= \left(\frac{d\tau_\mathrm{r}^*(\omega_\mathrm{r})}{d\omega_\mathrm{r}}|_{\omega_\mathrm{r}=\omega_0}\,\omega_\mathrm{r} - d_\mathrm{r}\,\omega_\mathrm{r}\right)\frac{\eta_\mathrm{p}}{\bar{V}_\mathrm{p}}\\ \Delta_\mathrm{p}^* &= \underbrace{(2\,K_2\,\omega_0 - d_\mathrm{r})\,\frac{\eta_\mathrm{p}}{\bar{V}_\mathrm{p}}}_{K_{\omega r}}\,\omega_\mathrm{r}\end{aligned} \tag{34}$$

where the rotor speed linearization point is determined as $\omega_0 = \frac{\lambda^*\,\bar{v}}{R_\mathrm{r}}$.

An integral state acting on the pressure error is introduced such that the closed-loop system achieves unity dc-gain. The expression for the integral state is derived to be that given by

$$\begin{aligned}\dot{x}_\mathrm{int} &= \Delta p^* - \Delta p = K_{\omega r}\,\omega_\mathrm{r} - \Delta p\\ \dot{x}_\mathrm{int} &= \frac{x_\mathrm{int}(k+1) - x_\mathrm{int}(k)}{T_\mathrm{s}}\\ x_\mathrm{int}(k+1) &= \underbrace{\begin{bmatrix}K_{\omega r} & T_\mathrm{s} & -T_\mathrm{s}\end{bmatrix}}_{\mathbf{K}_\mathrm{y}} \underbrace{\begin{bmatrix}\omega_\mathrm{r}(k)\\ \Delta p(k)\end{bmatrix}}_{\mathbf{y}(k)} + x_\mathrm{int}(k)\end{aligned} \tag{35}$$

$$x_\mathrm{int}(k+1) = \underbrace{\mathbf{K}_\mathrm{y}\,\begin{bmatrix}\mathbf{C}_\mathrm{p} & \mathbf{0} & \mathbf{0}\end{bmatrix}}_{\mathbf{C}_\mathrm{y}}\,\mathbf{x}_\mathrm{t}(k) + x_\mathrm{int}(k)$$

The complete state model appended with an integral state becomes that given in Eq. (36), by combining Eqs. (33) and (35).

$$\begin{aligned}\underbrace{\begin{bmatrix}\mathbf{x}_\mathrm{t}(k+1)\\ x_\mathrm{int}(k+1)\end{bmatrix}}_{\mathbf{x}_\mathrm{s}(k+1)} &= \underbrace{\begin{bmatrix}\mathbf{A}_\mathrm{t} & \mathbf{0}\\ \mathbf{C}_\mathrm{y} & 1\end{bmatrix}}_{\mathbf{A}_\mathrm{s}} \underbrace{\begin{bmatrix}\mathbf{x}_\mathrm{t}(k)\\ x_\mathrm{int}(k)\end{bmatrix}}_{\mathbf{x}_\mathrm{s}(k)} + \underbrace{\begin{bmatrix}\mathbf{B}_\mathrm{t}\\ \mathbf{0}\end{bmatrix}}_{\mathbf{B}_\mathrm{s}} u_\mathrm{m}(k)\\ &+ \underbrace{\begin{bmatrix}\mathbf{G}_\mathrm{t}\\ \mathbf{0}\end{bmatrix}}_{\mathbf{G}_\mathrm{s}} \mathbf{w}(k) \quad \mathbf{y}_\mathrm{t}(k) = \underbrace{\begin{bmatrix}\mathbf{C}_\mathrm{t} & \mathbf{0}\end{bmatrix}}_{\mathbf{C}_\mathrm{s}} \mathbf{x}_\mathrm{s}(k) + \mathbf{v}(k)\end{aligned} \tag{36}$$

$\mathbf{v}(k)$ is a measurement noise vector describing potential sensor noise disturbances.

7 Controller synthesis

A deterministic and a stochastic optimal controller are designed, where the deterministic is a Linear Quadratic Regulator (LQR) and the stochastic is a Linear Quadratic Gaussian (LQG) controller. The LQG-control problem consists of two subproblems being the LQR-control problem and the LQE-estimator problem.

7.1 LQR optimal control design

Since the LQR-control problem is also a part of the LQG-control design, only the LQG-design is documented. For the LQR-controller the same design procedure is applied, but where the two disturbance states are truncated.

The LQR-control problem is to minimize the quadratic cost function given in Eq. (37) by providing the optimal control input $u_\mathrm{m}(k)$.

$$\mathcal{J} = \sum_{k=1}^{\infty}\left(\mathbf{x}_\mathrm{s}(k)^T\,\mathbf{Q}\,\mathbf{x}_\mathrm{s}(k) + u_\mathrm{m}(k)^T\,\mathbf{R}\,u_\mathrm{m}(k)\right) \tag{37}$$

where $\mathbf{R} = \mathbf{R}^T \geq \mathbf{0}$ and $\mathbf{Q} = \mathbf{Q}^T \geq \mathbf{0}$ are positive definite weighting matrices. The input weighting matrix $\mathbf{R}$ specifies the importance of minimizing the control effort, and the state weighting matrix $\mathbf{Q}$ specifies the importance of driving the states to zero. The feedback

control law $u_{\mathrm{m}}(k) = -\mathbf{K}\,\hat{\mathbf{x}}_{\mathrm{t}}(k) + K_{\mathrm{int}}\,x_{\mathrm{int}}$ has the optimal solution of the feedback gain vector given as

$$\mathbf{K}_{\mathrm{s}} = \left(\mathbf{B}_{\mathrm{s}}^{T}\,\mathbf{S}\,\mathbf{B}_{\mathrm{s}} + \mathbf{R}\right)^{-1}\,\left(\mathbf{B}_{\mathrm{s}}^{T}\,\mathbf{S}\,\mathbf{A}_{\mathrm{s}}\right) \tag{38}$$

where $\mathbf{K}_{\mathrm{s}} = \left[\mathbf{K}\ K_{\mathrm{int}}\right]$ is the feedback gain vector. $\mathbf{S} = \mathbf{S}^{T} \geq \mathbf{0}$ is the unique positive-semi-definite solution to the Ricatti equation given by

$$\begin{aligned}\mathbf{0} &= \mathbf{A}_{\mathrm{s}}^{T}\,\mathbf{S}\mathbf{A}_{\mathrm{s}} - \mathbf{S} + \mathbf{Q} \\ &\quad - \left(\mathbf{A}_{\mathrm{s}}^{T}\,\mathbf{S}\,\mathbf{B}_{\mathrm{s}}\right)\,\left(\mathbf{B}_{\mathrm{s}}^{T}\,\mathbf{S}\,\mathbf{B}_{\mathrm{s}} + \mathbf{R}\right)^{-1}\,\left(\mathbf{B}_{\mathrm{s}}^{T}\,\mathbf{S}\,\mathbf{A}_{\mathrm{s}}\right)\end{aligned} \tag{39}$$

The state weighting matrix has been specified relative to an input weighting matrix chosen as $\mathbf{R} = 1$. With the objective of minimizing the reference tracking error, the integral state is weighted high, resulting in $\mathbf{Q} = \mathrm{diag}\left\{\left[0\ 0\ \cdots\ 0\ 10\right]\right\}$. For both the LQG and LQR-controllers, a weighting of 10 on the integral state and 0 for all other states is chosen. As a result, the control problem has been reduced significantly from being rather complicated to tuning of a single parameter, being the weighting of the integral state.

7.2 LQE optimal state estimation

The optimal state estimation is done by use of a discrete Kalman filter having the state equation given by.

$$\begin{aligned}\hat{\mathbf{x}}_{\mathrm{t}}(k+1) &= \mathbf{A}_{\mathrm{t}}\,\hat{\mathbf{x}}_{\mathrm{t}}(k) + \mathbf{B}_{\mathrm{t}}\,u_{\mathrm{m}}(k) + \mathbf{L}\,\left(\mathbf{y}_{\mathrm{t}}(k) - \hat{\mathbf{y}}(k)\right) \\ \hat{\mathbf{y}}(k) &= \mathbf{C}_{\mathrm{t}}\,\hat{\mathbf{x}}_{\mathrm{t}}(k)\end{aligned} \tag{40}$$

The optimal estimation problem is to determine the Kalman filter gain $\mathbf{L}$, which minimize the variance of the state estimation error expressed as

$$\mathcal{J} = E\left\{\left(\mathbf{x}_{\mathrm{t}}(k) - \hat{\mathbf{x}}_{\mathrm{t}}(k)\right)^{T}\,\left(\mathbf{x}_{\mathrm{t}}(k) - \hat{\mathbf{x}}_{\mathrm{t}}(k)\right)\right\} \tag{41}$$

The noise covariance matrices necessary for designing the LQG controller is provided in Eq. (42). It is assumed that there is no cross-correlation between the state noise $\mathbf{w}$ and the measurement noise $\mathbf{v}$.

$$E\left\{\mathbf{w}(k)\,\mathbf{w}(k)^{T}\right\} = \mathbf{W} \quad E\left\{\mathbf{v}(k)\,\mathbf{v}(k)^{T}\right\} = \mathbf{V} \tag{42}$$

The optimal solution to the Kalman filter may be derived to be that given by

$$\mathbf{L} = \mathbf{A}_{\mathrm{t}}\,\mathbf{P}\,\mathbf{C}_{\mathrm{t}}^{T}\,\left(\mathbf{C}_{\mathrm{t}}\,\mathbf{P}\,\mathbf{C}_{\mathrm{t}}^{T} + \mathbf{V}\right)^{-1} \tag{43}$$

where the matrix $\mathbf{P} = \mathbf{P}^{T} \geq \mathbf{0}$ is the unique positive-semi-definite solution to the steady-state Ricatti equation given by

$$\begin{aligned}\mathbf{0} &= \mathbf{A}_{\mathrm{t}}\,\mathbf{P}\,\mathbf{A}_{\mathrm{t}}^{T} - \mathbf{P} + \mathbf{G}_{\mathrm{t}}\mathbf{W}\,\mathbf{G}_{\mathrm{t}}^{T} \\ &\quad - \mathbf{A}_{\mathrm{t}}\,\mathbf{P}\,\mathbf{C}_{\mathrm{t}}^{T}\,\left(\mathbf{C}_{\mathrm{t}}\,\mathbf{P}\,\mathbf{C}_{\mathrm{t}}^{T} + \mathbf{V}\right)^{-1}\,\mathbf{C}_{\mathrm{t}}\,\mathbf{P}\,\mathbf{A}_{\mathrm{t}}^{T}\end{aligned} \tag{44}$$

A measurement noise of $e = 1\ \%$ has been assumed for both the pressure and rotor speed, while no measurement noise is present for the binary motor states. As a result, the measurement noise covariance matrix becomes $\mathbf{V} = \mathrm{diag}\left\{\left[e^2\ e^2\ 0\ \cdots\ 0\right]\right\}$.

The state covariance matrix is obtained by finding the power of the disturbance states. The power in the quantizer error state is found in Eq. (19) to be Q_{d}. The power in the aerodynamic torque state is identified from the discrete algebraic Lyapunov equation given by

$$\mathbf{A}_{\mathrm{p}}\,Q_{\tau}\,\mathbf{A}_{\mathrm{p}}^{T} - Q_{\tau} + \mathbf{G}_{\mathrm{p}}\,\Pi_{\tau}\,\mathbf{G}_{\mathrm{p}}^{T} = 0 \tag{45}$$

where $\Pi_{\tau} = 1$ is the white noise intensity. As a result the state noise covariance matrix becomes $\mathbf{W} = \mathrm{diag}\left\{\left[Q_{\tau}\ Q_{\mathrm{d}}\right]\right\}$.

A block diagram representation of the LQG closed-loop control system is shown in Fig. 13. In the LQR case, no estimator and noise inputs are present and the designed controller acts directly on the measured states.

8 Simulation results

The performance of the optimal controllers is investigated by simulation in the nonlinear dynamic model of the NREL 5-MW turbine including the DFP transmission and using the generated full-field flow wind profiles as input. Additionally, the performance of the optimal controllers is compared to that of the NREL PI-controller, with a conventional transmission system described in [17]. The simulation results are shown in Fig. 14 for a mean wind speed input of 8 m/s. It is seen that the output response using the three different controllers are quite similar. The results reveal that the

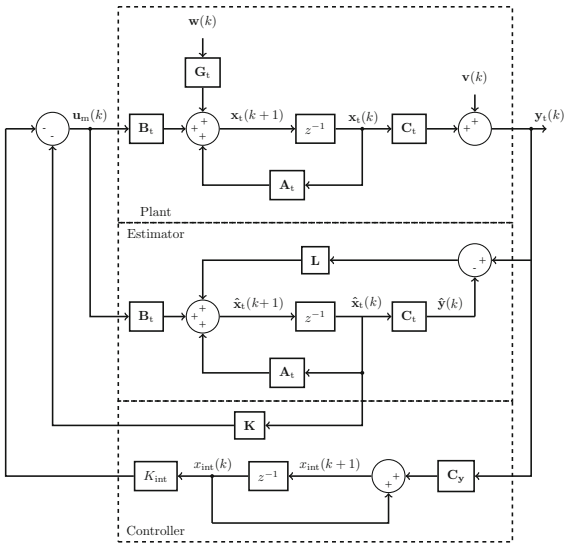

Fig. 13 Block diagram of the LQG-controller

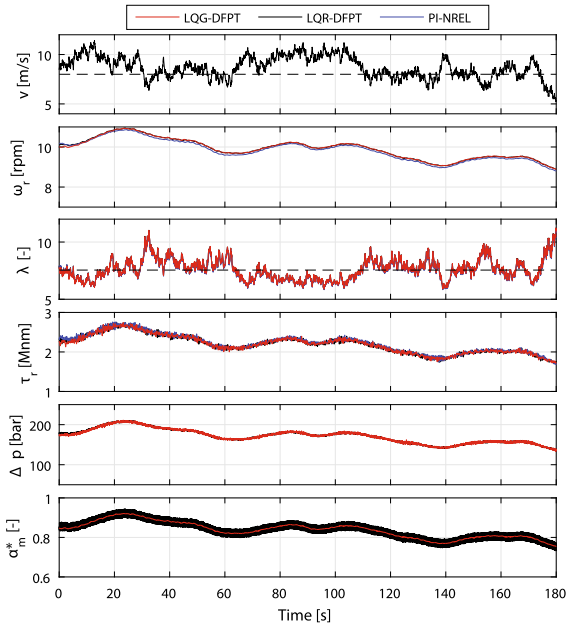

Fig. 14 Simulation results for NREL 5 MW turbine with turbulent wind profile, $\bar{v} = 8\ m/s$

rotor speed using the PI-controller has a minor offset with respect to the optimal controllers. This is caused by the gain used in the $K\ \omega^2$ control law which is not the precise optimal one in the NREL PI-controller. For a clearer view and to compare the pressure tracking performance of the two optimal controllers, a zoomed view of the pressure difference is shown in Fig. 15.

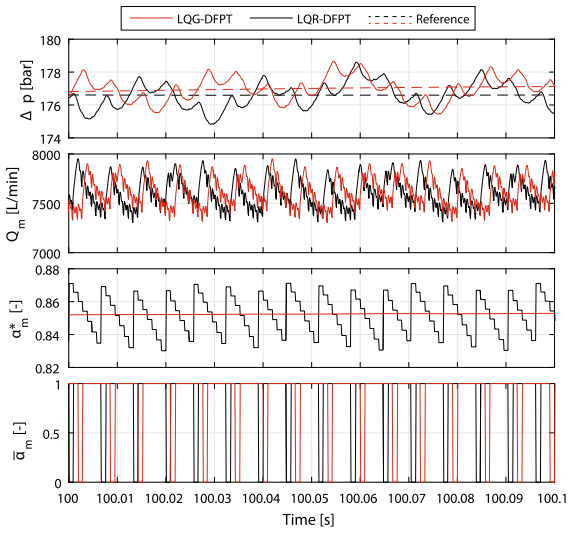

Fig. 15 Zoomed view of simulation results for NREL 5 MW turbine with turbulent wind profile, $\bar{v} = 8\ m/s$

The simulation results shows that both controllers have a great pressure tracking performance with a maximum pressure error of $\approx$ 2 bar. No tracking performance improvement has thus been obtained by including the wind and quantization disturbances. The stepwise behavior of the LQR-control signal, α^*_{m}, is not seen for the LQG-controller, since the estimated states are not limited to being binary. The significantly smoother control signal is, however, quantized afterward, why it does not contribute to an improved transient performance. An improved disturbance rejection might have been obtained, but the shown simulation results are inconclusive with respect to this. It is expected that an improved disturbance rejection may be obtained with a LQG-controller if an integral state is not added to the system, but this has not been investigated. Both controllers have similar fluctuations in the pressure response with an amplitude in the range of $\pm$ 2 bar. The pressure fluctuations are a direct result of the large peak in the motor flow due to the activation of a single additional pressure chamber. It is therefore assessed that a significant increase in tracking performance and reduction in torque fluctuations are hardly achieved control wise. Instead a hydraulic accumulator and/or a partial stroke operation strategy is expected to improve the transient performance. It should be noted that a partial stroke operation entails several difficulties, since a time varying model is obtained with the presented approach (or a vague linear approximation at a displacement frac-

tion) and the valve closing angles has to be estimated for every actuation.

9 Conclusion

In this paper, a control strategy for a full stroke operated digital displacement machine is presented. In the proposed control strategy, a model-based design approach for feedback control of a digital transmission-based variable-speed wind turbine is developed. A linearization method of handling the combination of nonlinear continuous dynamics with discretely updated binary inputs is given and allows for use of linear control theory. A stochastic (LQG) and a deterministic (LQR) optimal controller have been synthesized, with the objective of accurate pressure reference tracking for optimal energy extraction. Simulation results reveal that both controllers are able to track the optimal rotor speed similar to a conventional transmission with corresponding controller. It is therefore rendered probably that it is possible to utilize linear model-based feedback control for such system with nonlinear continuous, discrete, binary and stochastic effects. The LQG-controller with disturbance compensation does not improve the tracking performance compared to the LQR-controller under the tested conditions. This indicates that the simpler LQR-controller with integral state is sufficient for accurate tracking performance. It is assessed that a significant improvement in tracking performance and torque fluctuation reduction is hardly achievable simply by control if a full stroke operation strategy is used without a hydraulic accumulator.

Acknowledgements This research was funded by the Danish Council for Strategic Research through the HyDrive project at Aalborg University, at the Department of Energy Technology (case no. 1305-00038B).

References

1. Armstrong, B.S.R., Yuan, Q.: Multi-level control of hydraulic gerotor motor and pumps. In: Proceedings of the 2006 American Control Conference, Minneapolis, Minnesota, USA (June 2006)
2. Chapple, P., Lindholdt, P.N., Larsen, H.B.: An approach to digital distributor valves in low speed pumps and motors. ASME/BATH 2014 Symposium on Fluid Power and Motion Control, Bath, United Kingdom (2014)
3. Commission, I.E.: International Standard, IEC 61400-1 3rd edition (2005)
4. Das, S., Pan, I.: Fractional Order Signal Processing: Introductory Concepts and Applications. Springer, Berlin. ISBN 978-3-642-23117-9 (2012)
5. Dolan, B., Aschemann, H.: Control of a wind turbine with a hydrostatic transmission an extended linearisation approach. In: 17th International Conference on Methods and Models in Automation and Robotics (2012)
6. Han, H.Y., Wang, J., Huang, Q.X.: Analysis of unsymmetrical valve controlling unsymmetrical cylinder stability in hydraulic leveler. Nonlinear Dyn. **70**, 1199–1203 (2012)
7. Hansen, A.H., Pedersen, H.C.: Energy cost of avoiding pressure oscillations in a discrete fluid power force system. In: Proceedings of the ASME/BATH 2015 Symposium on Fluid Power and Motion Control, FPMC, American Society of Mechanical Engineers, pp. 1–10 (2015)
8. Hansen, A.H., Pedersen, H.C.: Optimal configuration of discrete fluid power force system utilised in the pto for wecs. Ocean Eng. **117**(OE3694), 88–98 (2016)
9. Hansen, A.H., Pedersen, H.C.: Reducing pressure oscillations in discrete fluid power systems. Proc. Part I J. Syst. Control Eng. **230**(10), 1093–1105 (2016)
10. Heikkila, M., Linjama, M.: Displacement control of a mobile crane using digital hydraulic power management system. Mechatronics **23**(4), 452–461 (2013)
11. Hoven, V.D.: Power spectrum of horizontal wind speed in the frquency range from 0.0007 to 900 cycles per hour. J. Atmos. Sci. **14**, 160–164 (1957)
12. Jin, Y., Luo, X.: Stochastic optimal active control of a half-car nonlinear suspension under random road excitation. Nonlinear Dyn. **72**, 185–195 (2013)
13. Johansen, P., Roemer, D.B., Pedersen, H.C., Andersen, T.O.: Delta-sigma modulated displacement of a digital fluid power pump. In: Proceedings of the 7th Workshop on Digital Fluid Power. LCM GmbH. s. The Seventh Workshop on Digital Fluid Power, Linz, Austria, pp. 1–9. (2015)
14. Johansen, P., Roemer, D.B., Pedersen, H.C., Andersen, T.O.: Discrete linear time invariant analysis of digital fluid power pump flow control. J. Dyn. Syst. Measurement and Control Trans. ASME **139**(10), 101007 (2017)
15. Jonkman, B.J.: TurbSim Users Guide: Version 1.50, National Renewable Energy Laboratory, US Department of Energy (2009)
16. Jonkman, B.J.: Overview of the TurbSim Stochastic Inflow Turbulence Simulator, National Renewable Energy Laboratory. US, Department of Energy (2009)
17. Jonkman, J.M., Butterfield, S., Musial, W., Scott, G.: Definition of a 5-mw reference wind turbine for offshore system development (2009)
18. Jrf, A., Minav, T., Pietola, M.: Nonsymmetrical flow compensation using hydraulic accumulator in direct driven differential cylinder application. In: Proceedings of the 9th FPNI PhD Symposium on Fluid Power, Florianpolis, Brazil (2016)
19. Kaimal, J.C., Wyngaard, J.C., Izumi, Y., Cote, O.R.: Spectral characteristics of surface-layer turbulence. Q. J. R. Meteorol. Soc. **98**, 563–589 (1972)
20. Kalbat, A.: Linear quadratic gaussian (lqg) control of wind turbines. In: Proceddings of the 3rd International Conference on Electric Power and Energy Conversion Systems (2013)
21. Laguna, A.J., Diepeveen, N.F.B., van Wingerden, J.W.: Analysis of dynamics of fluid power drive-trains for variable

speed wind turbines: parameter study. IET Renew. Power Gener. **8**(4), 398–410 (2014)
22. M. Ehsan, W.R., Salter, S.: Modeling of digital-displacement pump-motors and their application as hydraulic drives for nonuniform loads. J. Dyn. Syst. Measurement and Control **122**, 210–215 (2000)
23. Mateescu, R., Pintea, A., Stefanoiu, D.: Discrete-time lqg control with disturbance rejection for variable speed wind turbines. In: Proceedings of the 1st International Confeference on System and Computer Science, Lille, France, pp. 1–6. (2012)
24. Ming, Z., Hong, N., Rupeng, Z.: Stochastic optimal control of flexible aircraft taxiing at constant or variable velocity. Nonlinear Dyn. **62**, 485–497 (2010)
25. Mitsubishi Heavy Industries, L.: Wind turbine generator and tidal current generator and operation method thereof, Patent: US 20120104752 A1, 2012 (2013)
26. Mitsubishi Heavy Industries, L.: Power generating apparatus of renewable energy type and operation method thereof, Patent: US 20130214537 (2013)
27. Mitsubishi Heavy Industries, L.: Power generating apparatus of renewable energy type and method of operating the same, Patent: US 20130307493 A1 (2013)
28. Mitsubishi Heavy Industries, L.: Energy extraction device, group of energy extraction devices and operating methods, Patent: US 20130221676 A1 (2013)
29. Mitsubishi Heavy Industries, L.: Hydraulic transmission, power generating apparatus of renewable energy type, and operation method thereof, Patent: EP 2899432 A2 (2015)
30. Mitsubishi Heavy Industries, L.: Hydraulic transmission comprising variable displacement pump or motor operable with discontinuous range of displacements, Patent: EP 2649348 A1 (2015)
31. Noergaard, C., Bech, M.M., Roemer, D.B., Schmidt, L.: Experimental validation of modelled fluid forces in fast switching hydraulic on/off valves. In: Proceedings of the 2015 International Conference on fluid power and Mechatronics (FPM), IEEE Press, pp. 68–73 (2015)
32. Payne, G.S., Kiprakis, A.E., Ehsan, M., Rampen, W., Chick, J.P., Wallace, A.R.: Efficiency and dynamic performance of digital displacement hydraulic transmission in tidal current energy converters. J. Power and Energy Proc. IMechE Part A **221**, 207–218 (2007)
33. Payne, G.S., Stein, U.P.P., Ehsan, M., Caldwell, N.J., Rampen, W.H.S.: Potential of digital displacement hydraulics for wave energy conversion. In: Proceedings of the 6th European Wave and TIdal Energy Conference, Glasgow UK. (2005)
34. Pedersen, H.C., Hansen, R.H., Hansen, A.H., Andersen, T.O., Bech, M.M.: Design of full scale wave simulator for testing power take off systems for wave energy converters. Int. J. Mar. Energy **13**, 130–156 (2016)
35. Pintea, A., Christov, N., Borne, P., Popescu, D., Badea, A.: Optimal control of variable speed wind turbines. In: The 19th Mediterranean Conference on Control and Automation, Corfu, Greece (2011)
36. Rampen, W.: Gearless transmissions for large wind turbines—the history and future of hydraulic drives. Artemis IP Ltd, Scotland Artemis IP Ltd., Scotland
37. Rampen, W.: The development of digital displacement technology. In: Proceedings of Bath/ASME FPMC Symposium (2010)
38. Reiss, J.D.: Understanding sigma-delta modulation: The solved and unsolved issues. J. Audio Eng. Soc. **56**(1/2), 49–64 (2008)
39. Roemer, D.B.: Design and optimization of fast switching valves for large scale digital hydraulic motors. PhD thesis, Department of Energy Technology, Aalborg University (2014)
40. Roemer, D.B., Johansen, P., Pedersen, H.C., Andersen, T.O.: Design method for fast switching seat valves for digital displacement machines. In: Proceedings of the 8th FPNI PhD Symposium on Fluid Power (2014)
41. Roemer, D.B., Johansen, P., Pedersen, H.C., Andersen, T.O.: Optimum design of seat region in valves suitable for digital displacement machines. Int. J. Mechatron. Autom. **4**(2), 116–126 (2014)
42. Roemer, D.B., Johansen, P., Pedersen, H.C., Andersen, T.O.: Fluid stiction modeling for quickly separating plates considering the liquid tensile strength. J. Fluids Eng. **137**(6), 061205 (2015)
43. Roemer, D.B., Johansen, P., Pedersen, H.C., Andersen, T.O.: Optimum design of moving coil actuator for fast-switching valves in digital hydraulic pumps and motors. IEEE ASME Trans. Mechatron. **20**(6), 2761–2770 (2015)
44. Roemer, D.B., Johansen, P., Schmidt, L., Andersen, T.O.: Modeling of movement-induced and flow induced fluid forces in fast switching valves. In: Proceedings of the 2015 International Conference on Fluid Power and Mechatronics (FPM). IEEE press, pp. 978–983 (2015)
45. Salter, S.H., Taylor, J.R.M., Caldwell, N.J.: Power conversion mechanisms for wave energy. Proc. Inst. Mech. Eng. Part M J. Eng. Marit. Environ. **216**(1), 1–27 (2002)
46. Scheidl, R., Manhartsgruber, B.: On the dynamic behavior of servo-hydraulic drives. Nonlinear Dyn. **17**, 247–268 (1998)
47. Scheidl, R., Manhartsgruber, B.: State of the art in hydraulic switching control—componets, systems, applications. In: Proceedings of the 9th Scandinavian International Conference on Fluid Power (2005)
48. Schmidt, L., Roemer, D.B., Pedersen, H.C., Andersen, T.O.: Speed-variable switched differential pump system for direct operation of hydraulic cylinders. In: Proceedings of ASME/BATH 2015 Symposium on Fluid Power and Motion Control, American Society of Mechanical Engineers (2015)
49. Sniegucki, M., Gottfried, M., Klingauf, U.: Optimal control of digital hydraulic drives using mixed-integer quadratic programming. In: 9th IFAC Symposium on Nonlinear Control Systems (2013)
50. Song, X.: Modeling an active vehicle suspension system with application of digital displacement pump motor. In: Proceedings of the ASME 2008 International Design Engineering Techical Conference/Computers and Information in Enegineering Conference, Brooklyn - New York, Vol. 5, pp. 749–753 (2008)
51. Tahavori, M., Leth, J., Kallese, C., Wisniewski, Rafael: Optimal control of nonlinear hydraulic networks in the presence of disturbance. Nonlinear Dyn. **75**, 539–548 (2013)
52. Vepa, R.: Dynamic Modeling, Simulation and Control of Energy Generation. Springer, Berlin. ISBN 978-1-4471-5400-6 (2013)

53. Wadsley, L.: Optimal system solutions enabled by digital pumps. International Exposition for Power Transmission, Las Vegas (2011)
54. Wang, F., Stelson, K.A.: Model predictive control for power optimization in a hydrostatic wind turbine. In: 13th Scandinavian International Conference on Fluid Power, Linkping, Sweden (2013)
55. Wilfong, G., Batdorff, M., Lumkes, J.: Design and dynamic analysis of high speed on/off poppet valves for digital pump/motors. In: Proceedings of the 6th FPNI-PhD Symposium (2010)
56. Wilfong, G., Holland, M., Lumkes, J.: Design and analysis of pilot operated high speed on/off valves for digital pump/motors. In: Proceedings of the 52nd National Conference on Fluid Power (2011)
57. Winkler, B.: Development of a fast low-cost switching valve for big flow rates. In: Proceedings of the 3rd FPNI PhD symposium on Fluid Power (2004)
58. Winkler, B., Ploeckinger, A., Scheidl, R.: Components for digital and swithcing hydraulics. In: Proceedings of 1st Workshop on Digital Fluid Power (2008)
59. Winkler, B., Scheidl, R.: Optimization of a fast switching valve for big flow rates. In: Proceedings of the Bath Workshop on Power Transmission and Motion Control (2006)
60. Zhu, Y., Jiang, W.L., Kong, X.D., Zheng, Z.: Study on nonlinear dynamics characteristics of electrohydraulic servo system. Nonlinear Dyn. **80**, 723–737 (2015)